ADVANCED FUNCTIONAL MATERIALS
www.afm-journal.de

Impact of Defects and Disorder on the Stability of Ta_3N_5 Photoanodes

Lukas M. Wolz, Gabriel Grötzner, Tim Rieth, Laura I. Wagner, Matthias Kuhl, Johannes Dittloff, Guanda Zhou, Saswati Santra, Verena Streibel, Frans Munnik, Ian D. Sharp, and Johanna Eichhorn**

The photoelectrochemical performance of Ta_3N_5 photoanodes is strongly impacted by the presence of shallow and deep defects within the bandgap. However, the role of such states in defining stability under operational conditions is not well understood. Here, a highly controllable synthesis approach is used to create homogenous Ta_3N_5 thin films with tailored defect concentrations to establish the relationship between atomic-scale point defects and macroscale stability. Reduced oxygen contents increase long-range structural order but lead to high concentrations of deep-level states, while higher oxygen contents result in reduced structural order but beneficially passivate deep-level defects. Despite the different defect properties, the synthesized photoelectrodes degrade similarly under water oxidation conditions due to the formation of a surface oxide layer that blocks interfacial hole injection and accelerates charge recombination. In contrast, under ferrocyanide oxidation conditions, it is found that Ta_3N_5 films with high oxygen concentrations exhibit long-term stability, whereas those possessing lower oxygen contents and higher deep-level defect concentrations rapidly degrade. These results indicate that deep-level defects result in rapid trapping of photocarriers and surface oxidation but that shallow oxygen donors can be introduced into Ta_3N_5 to enable kinetic stabilization of the interface.

1. Introduction

During the last decade, transition metal nitride semiconductors have emerged as interesting materials for use as photoelectrodes in solar fuel generators.[1–4] Compared to oxides, nitrides enable more efficient visible light harvesting due to their reduced bandgaps,[5,6] while also providing higher charge carrier mobilities that arise from enhanced metal-nitrogen bond covalency.[2] Within this class, the most intensively investigated photoanode material is Ta_3N_5, which offers a bandgap of 2.1 – 2.2 eV, favorable band alignment for water oxidation, and a theoretical saturation photocurrent density of 10.6 – 12.5 mA cm^{-2}.[7–9] Despite this collection of desirable properties, pure Ta_3N_5 photoanodes often suffer from high onset potentials, low photocurrent densities, and poor stabilities under realistic reaction conditions. These critical performance limitations primarily stem from the presence of intrinsic point defects and impurities that are often poorly controlled during synthesis and can dominate the properties of functional photoelectrodes.[3,10–14] Intensive research efforts have mitigated some of these limitations by nanostructuring,[15,16] catalyst-functionalization,[9,17–19] contact optimization,[17,20] and/or doping[21–23] to realize high photocurrent densities and/or low onset potentials. However, for the development of rational material design strategies, particularly for achieving both high energy conversion efficiency and long-term stability, a basic understanding of the fundamental defect properties is essential.

The most commonly reported defects in Ta_3N_5 are substitutional oxygen impurities (O_N) and nitrogen vacancies (v_N), as well

L. M. Wolz, G. Grötzner, T. Rieth, L. I. Wagner, M. Kuhl, J. Dittloff, G. Zhou, S. Santra, V. Streibel, I. D. Sharp, J. Eichhorn
Walter Schottky Institute
Technische Universität München
Am Coulombwall 4, 85748 Garching, Germany
E-mail: sharp@wsi.tum.de; johanna.eichhorn@wsi.tum.de

The ORCID identification number(s) for the author(s) of this article can be found under https://doi.org/10.1002/adfm.202405532

DOI: 10.1002/adfm.202405532

L. M. Wolz, G. Grötzner, T. Rieth, L. I. Wagner, M. Kuhl, J. Dittloff, G. Zhou, S. Santra, V. Streibel, I. D. Sharp, J. Eichhorn
Physics Department
TUM School of Natural Sciences
Technische Universität München
Boltzmannstr. 10, 85748 Garching, Germany

F. Munnik
Institute of Ion Beam Physics and Materials Research
Helmholtz-Zentrum Dresden-Rossendorf
Bautzner Landstraße 400, 01328 Dresden, Germany

as associated reduced Ta centers (Ta^{3+}). In terms of their electronic properties, O_N is associated with the formation of shallow donor states that are responsible for the n-type conductivity of Ta_3N_5 and can have a positive impact on the photoelectrochemical (PEC) performance.[11,14] In contrast, v_N and Ta^{3+} states are reported to form deep levels that facilitate photocarrier trapping and charge carrier recombination, thus limiting the PEC performance.[9–11,14,24] Even for extrinsic impurity doped Ta_3N_5, the observed improvement in PEC performance is often assigned to the modulation of native and oxygen defect concentrations caused by the foreign atoms. For example, the dominating effect of doping Ta_3N_5 with Zr or La as electron acceptors has been associated with increased concentrations of O_N.[21–23] One exception to this behavior is Ti-doping, which has the benefit of reducing the concentration of deep-level defects and enhancing photocurrent densities without increasing the oxygen impurity content.[3] Furthermore, for catalyst or protection layer integration, the different defect properties of Ta_3N_5 can significantly impact the interface properties formed between the catalyst/protection layer and Ta_3N_5 and thus the resulting stability.[25]

While the impacts of O_N and v_N on the PEC performance of Ta_3N_5 photoanodes have been studied,[10–12,14] the role of these defects in defining (photo)electrochemical stability under operational conditions remains significantly less clear. For example, previous studies have elucidated the impact of different electrolytes on the stability of pure Ta_3N_5 photoelectrodes,[9,24,26] and investigated catalyst integration as a strategy to improve the stability.[9,17–19] However, these studies largely focused on optimizing the performance of Ta_3N_5 photoelectrodes. While significant progress in this direction has been made, the fundamental factors that underlie the stability of the material and its interfaces, particularly with respect to defect characteristics, remain poorly understood, thus limiting the ability to rationally design absorbers with intrinsically improved durability. Theoretical studies have predicted that v_N reduces mechanical stability and lattice cohesion, both in the bulk and at the surface, while O_N defects have the opposite effect and are beneficial for stabilizing the material.[27,28] However, Ta_3N_5 is commonly synthesized via ammonolysis of tantalum oxide,[10,11,29,30] resulting in simultaneous incorporation of high concentrations of both O_N and v_N defects. This poor control over defects has hindered systematic experimental studies that can independently resolve the roles of O_N and v_N in defining the stability of Ta_3N_5.

Here, we use a highly controllable synthesis approach to create compact Ta_3N_5 thin films with tailored O_N and v_N concentrations, thereby allowing us to establish the relationship between atomic-scale point defects and macroscale PEC performance and stability characteristics. Comprehensive comparative analysis of the resulting films reveals that low oxygen impurity concentrations lead to improved structural order but high concentrations of deep-level defect states detrimentally impact the optoelectronic properties. In contrast, higher oxygen impurity concentrations result in increased structural disorder but the beneficial passivation of such deep-level defects. Importantly, PEC stability tests reveal the immediate degradation of low oxygen-content Ta_3N_5 films, even in the presence of a hole scavenger, whereas oxygen-rich Ta_3N_5 photoelectrodes exhibit long-term stability under similar reaction conditions. These results show that the PEC stability strongly depends on the different defect properties of Ta_3N_5. Nevertheless, we also observe that all photoelectrodes undergo rapid degradation under water oxidation conditions in the absence of a hole scavenger or catalyst. Consistent with prior reports, analysis of the film and the electrolyte before and after PEC testing reveals that the photocurrent degradation is caused by the formation of a thin surface oxide layer that blocks interfacial hole injection and facilitates charge recombination.[9,24] Overall, the resistance of oxygen-rich Ta_3N_5 to surface oxidation under ferrocyanide hole scavenger oxidation conditions indicates the ability to kinetically stabilize the active semiconductor/electrolyte interface via defect engineering. In contrast, the larger deep-level defect concentrations present in low oxygen content films result in an unfavorable kinetic competition between interfacial charge injection and trapping-mediated self-oxidation reactions. Overall, these findings highlight the importance of tailoring point defects and foreign atom dopants in semiconductor photoelectrodes to not only enhance PEC performance characteristics but also increase stability via the application of kinetic stabilization strategies.

2. Results and Discussion

2.1. Synthesis of Ta_3N_5 Photoelectrodes from Different Precursors

A series of polycrystalline Ta_3N_5 thin films with controlled defect concentrations were synthesized using a two-step process (**Figure 1a**) that is analogous to the commonly applied ammonolysis of tantalum oxide at high temperatures.[10,29,30] First, (reactive) sputtering was used to deposit different precursor thin films with varying oxygen and nitrogen content. Specifically, we sputtered tantalum oxide (TaO_x), tantalum nitride (TaN_x), and elemental tantalum (Ta) films on silicon and fused silica substrates. Second, the sputtered films were converted into Ta_3N_5 by annealing in an NH_3 atmosphere with a constant flow of 100 sccm at 920 °C for 3 h. To enable reliable nitridation with minimal composition gradients, we synthesized Ta_3N_5 films with a thickness well below the optimal value required for achieving maximum photoelectrochemical current densities.[17] Moreover, we used highly doped Si substrates to enable elemental quantification without contributions from the support, despite the fact that they likely introduce additional back-contact resistances. While the three films are visually characterized by differing red and orange hues following annealing (Figure 1b), all exhibit the Raman spectrum of orthorhombic Ta_3N_5 (Figure 1c).[30,31] In the following, the synthesized Ta_3N_5 films are labeled according to the precursor thin film as Ta_3N_5(O), Ta_3N_5(N), and Ta_3N_5(Ta) for those derived from TaO_x, TaN_x, and Ta precursor films, respectively.

Chemical analysis of the precursor films confirmed that the dominant components are tantalum oxide (TaO_x), tantalum nitride (TaN_x), and lower tantalum oxidation states (Ta) (Figure S1, Supporting Information). Independent of the precursor composition (Table S1, Supporting Information), all conversion reactions generate H_2O and H_2 as by-products but in different amounts (Note S1, Supporting Information). This is in contrast to the conversion of stoichiometric Ta_2O_5 which only produces H_2O.[32] Interestingly, the conversion of TaN_x requires significantly less NH_3 and generates only small amounts of H_2O and H_2 compared to the conversion of non-nitride precursors. Generally, the conversion of TaO_x into Ta_3N_5(O) is associated

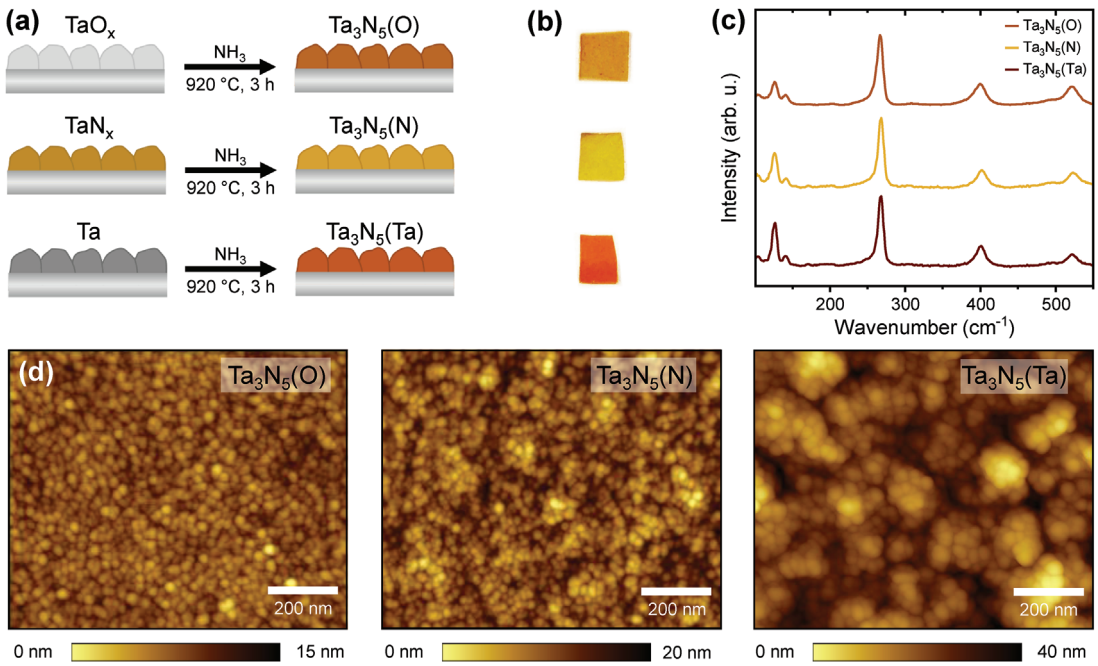

Figure 1. Schematic of the synthesis process, structure, and morphology of different Ta_3N_5 thin films. a) TaO_x, TaN_x, and Ta thin films were deposited by (reactive) sputtering and were subsequently converted to Ta_3N_5 by annealing at 920 °C in a constant NH_3 flow for 3 h. b) Optical images, c) Raman spectra, and d) topographic AFM images of the Ta_3N_5 photoelectrodes after NH_3 annealing for each of the three types of precursor films.

with an increase in mass density, leading to a volume contraction, while the conversion of TaN_x and Ta into Ta_3N_5(N) and Ta_3N_5(Ta), respectively, are characterized by a reduction in mass density, leading to a volume expansion. To balance these differences, the sputter processes for all three films were optimized to yield similar film thicknesses after NH_3 annealing, which was confirmed by elastic recoil detection analysis (ERDA). As shown in Figure 1d, atomic force microscopy (AFM) indicates that all three photoelectrodes exhibit a homogenous and compact topography, with increasing root mean square (RMS) roughness from 1.5 nm to 2.8 nm to 6.3 nm for Ta_3N_5(O) to Ta_3N_5(N) to Ta_3N_5(Ta). The much higher roughness of Ta_3N_5(Ta) likely arises from the large volume change during the NH_3 conversion step, which is the most significant among all three thin films.

2.2. Photoelectrochemical Performance and Stability

The PEC performance characteristics and stabilities were analyzed in 1 M phosphate buffer (KP_i, pH 12.3) with and without 0.1 M $K_4Fe(CN)_6$ as hole scavenger in the dark and under illumination (AM 1.5G, 100 mW cm^{-2}). With hole scavenger, all Ta_3N_5 films show negligible dark current, which excludes contributions from background currents and dark electrochemical corrosion (**Figure 2a**). A previous study without hole scavenger also revealed constant dark currents for low biases (<1.5 V versus reversible hydrogen electrode (RHE)) confirming material stability under dark conditions.[24]

Under illumination and in the presence of ferrocyanide, the photocurrent onset potential is observed at 0.6 V versus RHE for Ta_3N_5(N), 0.7 V versus RHE for Ta_3N_5(Ta), and 0.8 V versus RHE for Ta_3N_5(O). The photocurrent density at 1.23 V versus RHE is similar for all samples, with a value of ~0.6 mA cm^{-2}. In this context, it is important to note that the moderate photoelectrochemical performance observed in this study arises from the significantly lower film thickness compared to the optimal value of 800 nm for achieving maximum PEC efficiency,[17] as well as the non-ideal Si back contact. Nevertheless, the thickness and Si support were selected to ensure compositionally homogeneous thin films and enable precise elemental quantification necessary for deriving mechanistic insights. While Ta_3N_5(O) shows a steady increase of current with increasingly anodic potential, both Ta_3N_5(N) and Ta_3N_5(Ta) show indications of a photooxidation peak, which could indicate material degradation. This hypothesis is confirmed by chronoamperometry measurements, which reveal rapid degradation of Ta_3N_5(N) and Ta_3N_5(Ta) during the first 5 min of the experiment, whereas Ta_3N_5(O) is stable for at least 1 h (Figure 2b). Furthermore, after stability testing, the current-voltage characteristic of Ta_3N_5(O) remains unchanged (Figure 2c), while the photocurrent densities are significantly reduced and the onset potentials are anodically shifted for Ta_3N_5(N) and Ta_3N_5(Ta).

To provide additional insight into the relative stabilities of the different films, the PEC characteristics were measured in 1 M phosphate buffer in the absence of a hole scavenger. As expected considering the kinetically challenging oxygen evolution reaction (OER), all photoelectrodes exhibit significantly lower photocurrent densities (<0.3 mA cm^{-2} at 1.23 V versus RHE) and higher onset potentials. Interestingly, material degradation is observed for all three photoelectrodes (Figure S2, Supporting Information), with only a slightly slower degradation rate for Ta_3N_5(O)

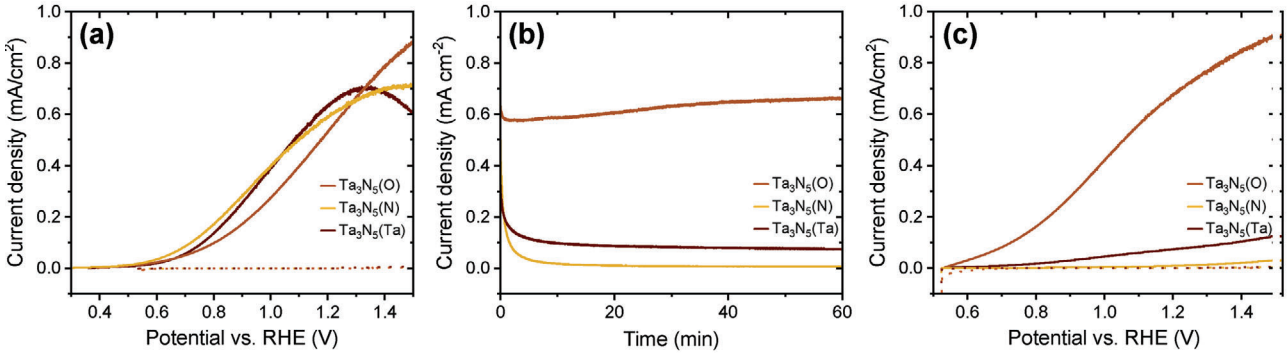

Figure 2. Photoelectrochemical characteristics of Ta_3N_5 thin films as a function of the different thin film precursors used for their synthesis. a) Linear sweep voltammetry (LSV), b) chronoamperometry at 1.23 V versus RHE, and c) linear sweep voltammetry after 1 h of chronoamperometric stability testing of Ta_3N_5(O), Ta_3N_5(N), and Ta_3N_5(Ta) photoelectrodes. The photoelectrochemical measurements were recorded in 1 M phosphate buffer (pH 12.3) in the presence of 0.1 M $K_4Fe(CN)_6$ as a hole scavenger under front side illumination (AM 1.5G, 100 mW cm^{-2}). Dotted lines correspond to LSV measurements in the dark.

compared to Ta_3N_5(N) and Ta_3N_5(Ta). After stability testing without a hole scavenger, all photoelectrodes are severely degraded and generate only small photocurrent densities (<30 μA cm^{-2} at 1.23 V versus RHE).

The observed enhanced stability of Ta_3N_5(O) in the presence of a hole scavenger suggests that this material can be kinetically stabilized against degradation under PEC conditions, while the Ta_3N_5(N) and Ta_3N_5(Ta) films remain unstable even upon rapid hole extraction. To the best of our knowledge, only the stability of Ta_3N_5(O) has been previously investigated under (photo)electrochemical conditions as a function of different hole scavengers.[24] Similar to our results, stable operation was uniquely reported for ferrocyanide oxidation.[9,24] In the absence of ferrocyanide as a hole scavenger, the photocurrent decrease was assigned to the formation of an amorphous surface oxide.[9] It has been shown that the formed surface states trap holes and electrons, leading to increased recombination rates at the surface.[24] However, the underlying reason for the unique stabilizing effect of ferrocyanide oxidation is still unclear. Importantly, our results show for the first time that the photoelectrochemical stability for ferrocyanide oxidation also strongly depends on the different material and defect properties introduced by the use of different thin film precursors. In the following, we seek to identify the key characteristics that lead to this enhanced stability of the Ta_3N_5(O) film. Given the potentially key role of kinetic stabilization mechanisms for achieving robust Ta_3N_5 photoanodes, such insights are of significant importance for the rational development of corrosion protection and catalyst integration strategies.

2.3. Bulk and Surface Chemical Composition Analysis

To understand the underlying reason for the variation in PEC stability as a function of the synthetic route, the bulk and surface chemical compositions of the synthesized Ta_3N_5 thin films were analyzed by ERDA and X-ray photoelectron spectroscopy (XPS), respectively. While ERDA was only conducted on as-synthesized Ta_3N_5 films, we used XPS to also determine the surface chemical compositions before and after PEC stability testing with and without a hole scavenger (**Table 1**). Among the three thin films, Ta_3N_5(O) has the highest bulk O/Ta ratio (0.10), while it is reduced for Ta_3N_5(N) (0.07), and Ta_3N_5(Ta) (0.05). Furthermore, the N/Ta ratio increases in the bulk from 1.59 for Ta_3N_5(O) to 1.68 for Ta_3N_5(Ta) and 1.75 for Ta_3N_5(N). In short, the composition of Ta_3N_5(Ta) is closest to the ideal stoichiometry of Ta_3N_5, while Ta_3N_5(O) is characterized by increased oxygen content and Ta_3N_5(N) by increased nitrogen content. Compared to the bulk composition, the surface nitrogen content is lower and oxygen content is higher for all samples, as determined by XPS. Despite this difference, the XPS data follow the composition trends observed by ERDA (Table 1), with the higher surface oxygen content arising from the formation of a thin surface oxide layer upon exposure to air.

Overall, the variations of N/Ta and O/Ta elemental ratios as a function of the thin film precursor agree well with previous studies. For example, Ta_3N_5 thin films synthesized via oxide-to-nitride conversion are typically characterized by N/Ta ratios of 1.1 – 1.5 and O/Ta ratios of 0.2 –:1.3.[13,33,34] In contrast, pure nitride-based processes, such as nitridation of tantalum

Table 1. Bulk and surface composition of different Ta_3N_5 thin films determined by ERDA and XPS, respectively. The PEC stability was tested in 1 M phosphate buffer (KP_i, pH 12.3) with 0.1 M $K_4Fe(CN)_6$ under illumination for 1 h.

SAMPLE	ERDA BEFORE PEC					XPS BEFORE PEC		XPS AFTER PEC	
	Ta [at.%]	N [at.%]	O [at.%]	N/Ta	O/Ta	N/Ta	O/Ta	N/Ta	O/Ta
Ta_3N_5(O)	35.9	57.0	3.5	1.59	0.10	1.50	0.31	1.27	0.34
Ta_3N_5(N)	34.8	61.0	2.3	1.75	0.07	1.63	0.21	0.62	1.40
Ta_3N_5(Ta)	36.3	61.0	1.8	1.68	0.05	1.59	0.13	0.65	1.26

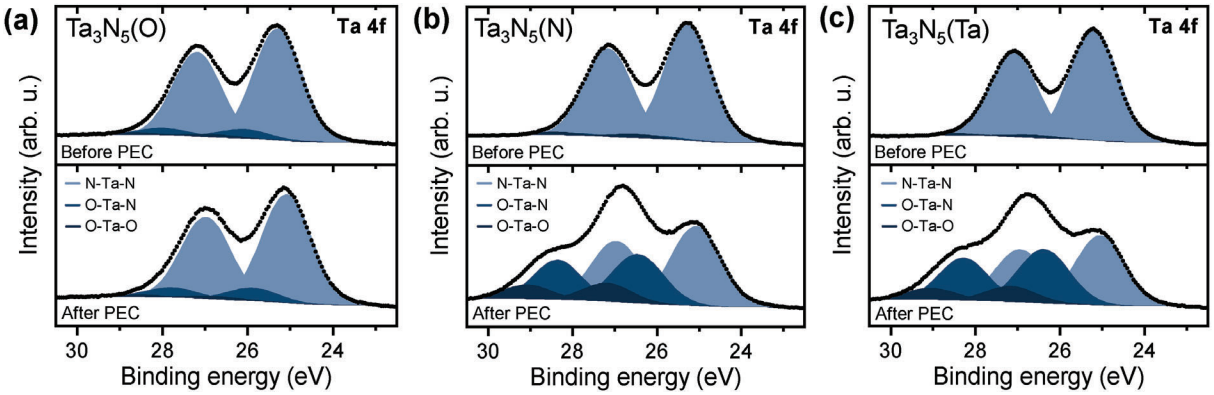

Figure 3. Surface chemical composition of Ta_3N_5 thin films on Si substrates before and after 1 h of chronoamperometry in 1 M KP_i with 0.1 M $K_4Fe(CN)_6$ under 1 sun (AM 1.5G) illumination, as indicated by Ta 4f core level spectra of a) Ta_3N_5(O), b) Ta_3N_5(N), and c) Ta_3N_5(Ta), which were synthesized by the nitridation of TaO_x, TaN_x, and Ta thin films, respectively.

nitride thin films, show increased N/Ta ratios of 0.5 – 1.8 and decreased O/Ta ratios of 0.1 – 0.6.[35–37] Interestingly, the oxygen content for Ta_3N_5(Ta) is lower than the lowest reported O/Ta ratio of 0.07 for Ta_3N_5(O), which was obtained after 120 h of NH_3 annealing.[38] This finding is consistent with previous analyses, which indicated that the oxygen content saturates at an appreciable level during the ammonolysis of oxide-based films, suggesting its incorporation into the forming nitride phase is energetically favored.[39,40] Thus, our work shows that starting from oxide-free precursors enables the fabrication of nitride films with significantly reduced oxygen content.

In addition to establishing the overall composition, we used XPS to analyze the chemical bonding state at the surface of each photoelectrode. **Figure 3** shows high-resolution Ta 4f core level spectra from films produced with the different precursors. Each spectrum can be deconvoluted into two spin-orbit split doublets, corresponding to tantalum nitride (bright blue) and oxynitride (blue), with Ta $4f_{7/2}$ peak positions at 25.1 eV and 25.8 eV, respectively. Ta_3N_5(Ta) shows the highest contribution (95%) from the tantalum nitride component, which is reduced to 91% for Ta_3N_5(N) and 87% for Ta_3N_5(O). The decreased tantalum nitride signals from the latter two samples correlate with increased tantalum oxynitride contributions in the Ta 4f regions, as well as increased tantalum oxide signal near 530.8 eV in the O 1s region (Figure S3, Supporting Information). However, the contribution of tantalum oxide (Ta $4f_{7/2}$ at 26.7 eV, dark blue) is near the sensitivity limit of our instrument.

To better understand the interfacial processes leading to the observed photocurrent degradation (Figure 2), we also used XPS to analyze the surface chemical composition after chronoamperometric PEC testing in the presence of 0.1 M $K_4Fe(CN)_6$ (Figure 3). Strikingly, this analysis reveals that the surface composition of Ta_3N_5(O) remains stable following sustained operation as a photoanode, whereas a significant increase of both the tantalum oxynitride and tantalum oxide contributions is observed for Ta_3N_5(N) and Ta_3N_5(Ta). Inspection of the O 1s (Figure S3, Supporting Information) and N 1s (Figure S4, Supporting Information) spectral regions further reveals an increase in tantalum oxide and a decrease in tantalum nitride contributions. Taken together, these findings indicate a stable surface condition for Ta_3N_5(O), but a replacement of lattice nitrogen by oxygen for Ta_3N_5(N) and Ta_3N_5(Ta), under PEC operating conditions with hole scavenger. In contrast, XPS reveals similar material degradation via oxidation for all three photoelectrodes when operated in the absence of a hole scavenger (Figure S5, Supporting Information), leading to N/Ta ratios of 0.5 – 0.6 and O/Ta ratios of 1.4 – 1.5. The observed formation of a tantalum oxynitride phase at the surface is in agreement with previous reports on the degradation of Ta_3N_5 without hole scavenger.[41,42] Furthermore, we find no indication of crystallinity of the formed surface oxide layer from grazing incidence X-ray diffraction (GI-XRD) measurements after the photoelectrochemical operation. While this observation does not allow an unambiguous assignment of the layer as being amorphous, it is consistent with a previous study, which confirmed the amorphous nature of the surface oxide via transmission electron microscopy (TEM).[9]

Surface oxidation introduces a large energetic barrier for interfacial transfer of photogenerated holes, blocking interfacial hole injection and facilitating charge recombination, thus reducing the photocurrent density. In this context, calculated energy band diagrams for increased surface oxide formation under dark and illuminated conditions revealed reduced photovoltage with increasing oxidation due to increased recombination in the oxidized layer.[24] Furthermore, it was previously reported that the electronic states generated by the surface oxide layer can pin the Fermi level near the middle of the bandgap, which further compromises the charge separation capability and leads to almost complete suppression of the photoactivity.[9] Nevertheless, we find appreciable resistance of Ta_3N_5(O) to surface oxidation under ferrocyanide oxidation conditions, which enables stable photocurrent densities during its long-term operation as a photoanode.

Additional insights into the photoelectrochemical degradation process are provided by inductively coupled plasma mass spectrometry (ICP-MS), which was used to analyze the electrolyte solutions after 1 h of chronoamperometry under illumination at 1.23 V versus RHE in 1 M KP_i with and without 0.1 M $K_4Fe(CN)_6$. For both conditions, we observe minimal loss of Ta into the electrolyte for all three photoelectrodes, with Ta dissolution corresponding to an equivalent thickness loss of ~0.1 nm to 0.5 nm. Accordingly, even without a hole scavenger, Ta dissolution is nearly negligible and is limited to a very thin surface

region. Furthermore, no significant change in surface morphologies (Figures S6 and S7, Supporting Information) or bulk structures (Figure S8, Supporting Information) of the Ta_3N_5 films are observed by AFM or GI-XRD, respectively, after PEC operation with and without hole scavenger. Specifically, we find no indication of crystallinity of the formed surface oxide layer from GI-XRD measurements (Figure S8, Supporting Information). While this observation does not allow an unambiguous assignment of the layer as being amorphous, it is consistent with a previous study, which confirmed the amorphous nature of the surface oxide via TEM analysis.[9] Overall, we conclude that the degradation of photocurrent density during chronoamperometric testing is not caused by continuous dissolution but is rather the result of surface oxidation. These findings agree with the self-limiting surface photooxidation process reported in previous work.[9] In stark contrast, the surface of Ta_3N_5(O) is stable against photooxidation during ferrocyanide oxidation, which lends support to the conclusion that oxygen impurities play a crucial role in stabilizing the Ta_3N_5/electrolyte interface.

As discussed above, stabilization of Ta_3N_5 surfaces in the presence of ferrocyanide has been previously reported and is likely due to a combination of its ability to rapidly extract photogenerated holes and its lack of oxygen-containing reaction intermediates.[9,24] However, our results indicate that its ability to prevent oxidative degradation is highly dependent on the synthetic route used to produce the material. Thus, we hypothesize that the defect or impurity content of the material plays a critical role in the stabilization mechanism. In this context, the Gerischer model of photocorrosion provides a valuable framework for assessing the thermodynamic and kinetic stabilities of illuminated semiconductors.[43] Specifically, a photoanode can only be considered thermodynamically stable against oxidation by photogenerated holes if its self-oxidation potential lies within its valence band. However, prior theoretical calculations have reported that the self-oxidation potential of Ta_3N_5 lies within the bandgap, close to its conduction band minimum.[44] While these calculated self-oxidation potentials can suffer from considerable uncertainties, this prediction is consistent with the rapid photodegradation observed during PEC measurements in the absence of a hole scavenger. However, to assess stability in the presence of a hole scavenger, it is also important to consider kinetics alongside thermodynamics. For the case that hole transfer to the redox couple in solution is significantly faster than the self-oxidation process, the surface can be kinetically stabilized. For the case of Ta_3N_5(O), it appears that the kinetics of ferrocyanide oxidation are faster than those associated with the degradation of the material itself. However, this is not the case for the other two photoelectrodes. This finding suggests that the trapping of holes by defects near the semiconductor/electrolyte interface may play an important role in defining its kinetically controlled stability. Thus, we now turn to a detailed assessment of the structural order and defect properties of each of the differently synthesized films.

2.4. Structure and Disorder in Ta_3N_5 Thin Films

To characterize the defects formed in the three Ta_3N_5 photoelectrodes, we next analyze the crystalline structures and optoelectronic properties in greater detail. Consistent with the Raman spectra presented above (Figure 1c), GI-XRD indicates that all three photoelectrodes form orthorhombic Ta_3N_5 (**Figure 4a**). However, the intensity ratios between the different reflections are different for Ta_3N_5(Ta) compared to Ta_3N_5(O) and Ta_3N_5(N), pointing toward a preferential orientation during growth. Nevertheless, since Ta_3N_5(O) and Ta_3N_5(N) possess similar thin film textures but very different photoelectrochemical stabilities, we can conclude that preferential film orientation does not play a dominant role in suppressing the oxidation of Ta_3N_5(O).

In terms of the structural quality of the different films, the total diffracted intensity is significantly larger for Ta_3N_5(Ta) compared to Ta_3N_5(O) and Ta_3N_5(N), which may indicate improved crystallinity. This finding is consistent with the different full width at half maximum (FWHM) values of the (023) diffraction peak at 31.6°, which has the smallest value of ~0.34° for Ta_3N_5(Ta) and broadens to ~0.38° for Ta_3N_5(N) and ~0.40° for Ta_3N_5(O). Generally, the broadening can arise from changes in crystal quality, crystallite size, and/or lattice strain. Using the Debye-Scherrer equation, we determined the average particle size to 24.1 nm, 21.6 nm, and 20.5 nm for Ta_3N_5(Ta), Ta_3N_5(N), and Ta_3N_5(O), respectively. The grain sizes observed by AFM (Figure 1d) follow a similar trend but are slightly larger, corresponding to a smaller expected FWHM in the GI-XRD data. These results indicate that material quality and/or strain also contribute to the observed peak broadening. Surprisingly, the Ta_3N_5(O) film possesses the lowest crystallinity and smallest grain size but the highest photoelectrochemical stability, which stands in contrast to many other materials in which enhanced stability is correlated with improved crystallinity.[45,46] Thus, we conclude that enhanced long-range structural order does not cause the observed improvement in stability for the Ta_3N_5 films investigated here, suggesting that the electronic character of the incorporated defects may play a dominant role in the photooxidation of this material.

2.5. Optical Properties and Electronically Active Defects

To understand how the choice of precursor impacts the defect properties and PEC stabilities of the resulting Ta_3N_5 films, we characterized their optical properties using photothermal deflection spectroscopy (PDS, Figure 4b) and photoluminescence spectroscopy (PL, Figure 4d). All three Ta_3N_5 thin films show a clear optical absorption onset at ~580 nm (Figure 4b). Using Tauc analysis of the recorded absorption spectra, we estimated the bandgaps of the Ta_3N_5 thin films to be 2.1 eV (Figure S9, Supporting Information), showing no significant change in the bandgap between the differently prepared photoelectrodes. Previous theoretical calculations have predicted that the optical and electronic bandgap of Ta_3N_5 first decreases and subsequently increases with increasing incorporation of oxygen.[47] However, for the rather small changes in oxygen concentrations present in our synthesized Ta_3N_5 films, the bandgaps reach a plateau and are approximately constant. This behavior is consistent with our observations, which indicate no significant change in the bandgap among the three different samples possessing different defect concentrations.

While the bandgaps of the Ta_3N_5 films produced from different precursors are approximately the same, PDS reveals

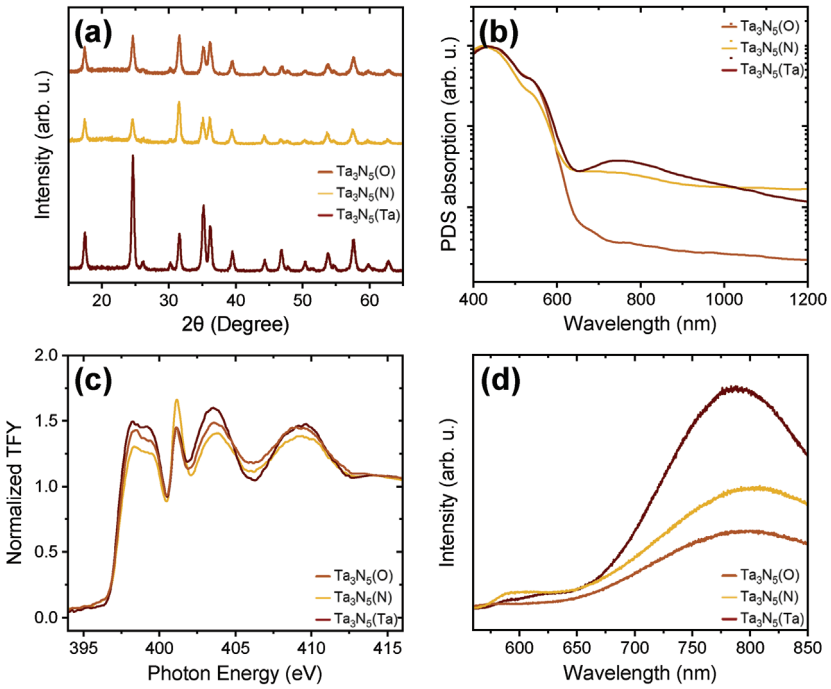

Figure 4. Optical and optoelectronic properties of different Ta_3N_5 films. a) GI-XRD, b) PDS, c) XAS of the N K-edge, measured in bulk-sensitive total fluorescence yield mode, and d) low-temperature (10 K) photoluminescence with 403 nm excitation for Ta_3N_5 (O), Ta_3N_5 (N), and Ta_3N_5 (Ta).

considerable changes in the sub-bandgap optical absorption characteristics (Figure 4b), indicating different defect properties. Interestingly, the Ta_3N_5(O) film is characterized by the weakest sub-bandgap absorption despite its comparatively high concentration of oxygen impurities, consistent with the shallow nature of O_N. In contrast, the sub-bandgap absorption strength is significantly increased for both Ta_3N_5(N) and Ta_3N_5(Ta), suggesting that these films possess considerably higher concentrations of optically active deep-level defects. Theoretical studies report in-gap states for the presence of v_N and low valent Ta^{3+} centers.[11,27,28,31,48] However, the densities-of-states of these in-gap states are still under discussion, with assignments to Ta 5d orbitals with minor contributions of N 2p orbitals,[48] localized electrons in v_N sites,[49] or to v_N and Ta^{3+} states,[11] which does not allow the relative contributions of v_N and Ta^{3+} to be distinguished at this time. Nevertheless, experimental studies show that the formation of such in-gap states can lead to enhanced trapping and recombination in Ta_3N_5 photoelectrodes.[9,11,24] While Ta_3N_5(N) and Ta_3N_5(Ta) possess similar sub-bandgap absorption strengths, we do observe differences in their spectral shapes. In particular, a pronounced peak near 750 nm is observed for Ta_3N_5(Ta) but is much weaker for Ta_3N_5(N). Both spectrally flat and peaked sub-bandgap absorption characteristics are frequently observed in Ta_3N_5 photoelectrodes,[10,12–14,22,23,48–50] though the underlying origin of these different spectral shapes remains under discussion. Here, spectral differences between Ta_3N_5(N) and Ta_3N_5(Ta) may indicate different relative concentrations or occupations of v_N and Ta^{3+} states, though it is not possible to make an unambiguous assignment. Indeed, we note that XPS provides no evidence for the presence of Ta^{3+} surface states in any of the three photoelectrodes, but their presence within the bulk cannot be excluded, as demonstrated by recent etching experiments.[11] Nevertheless, increased oxygen impurity concentrations are known to effectively passivate deep-level defect centers in Ta_3N_5,[48] which is consistent with our observation of a significantly reduced sub-bandgap absorption strength for Ta_3N_5(O).

While suppressed deep-level concentrations for O-containing films are observed, it is perhaps surprising that the Ta_3N_5(N), which has an excess of N, and Ta_3N_5(Ta), which has a near ideal stoichiometric composition, exhibit pronounced optical absorption from deep-level states typically associated with the presence of v_N. Thus, to better understand the nature of native defects in these films, we performed N K-edge X-ray absorption spectroscopy (XAS) in bulk-sensitive total fluorescence yield mode (TFY, Figure 4c). Overall, these measurements reveal similar spectral features that agree with both theoretical predictions[51] and previous experimental studies,[9,52] regardless of the synthesis pathway. However, one important difference is apparent: Ta_3N_5(N) shows a significantly stronger absorption peak at ~401 eV, which is characteristic of dinitrogen. The incorporation of dinitrogen during reactive sputtering of metal nitride films has been reported and was also correlated to such a spectral feature in the XAS spectrum.[53] Additionally, it was shown that dinitrogen incorporated during synthesis can remain present in the lattice even after subsequent NH_3 annealing.[54] In the present work, nitrogen was only added to the sputter gas mixture for the synthesis of Ta_3N_5(N), while Ar/O_2 and pure Ar were used for Ta_3N_5(O) and Ta_3N_5(Ta), respectively. These results indicate that dinitrogen is trapped in the lattice of Ta_3N_5(N), which can explain the measured over-stoichiometric N/Ta ratio by ERDA. Accordingly, the N/Ta ratio for Ta_3N_5(N) is not representative of the total amount of nitrogen incorporated into the lattice and, thus, v_N can also

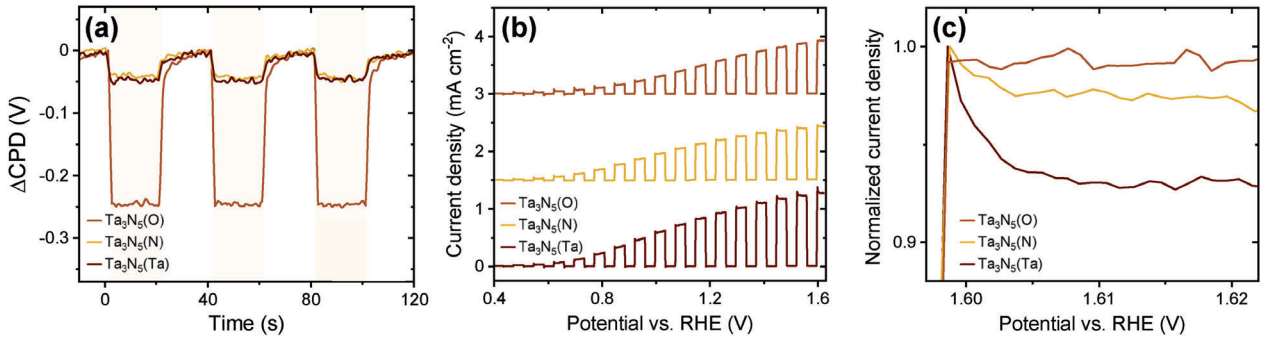

Figure 5. Impact of defect properties on charge separation and transfer. a) Change of the contact potential difference recorded as a function of time for repeated cycles of dark and illumination (yellow background) with 455 nm, providing a measure of the surface photovoltage. b) Linear sweep voltammetry in 1 M KP_i with hole scavenger under chopped AM 1.5G illumination at 100 mW cm^{-2}. The LSVs for the different Ta_3N_5 films are separated by an offset of 1.25 mA cm^{-2}. c) Zoom in on the normalized LSV data, highlighting the different current density overshoots upon illumination.

be present in the case of films exhibiting overall stoichiometric, and even over-stoichiometric, total nitrogen concentrations. This finding agrees with the PDS results discussed above, which provide evidence for high concentrations of deep-level states in the Ta_3N_5(N) film, despite its high nitrogen content.

Steady-state photoluminescence spectroscopy provides additional insight into the nature and impact of defects in the synthesized materials. For all Ta_3N_5 films, a broad emission band between 680 nm and 850 nm is observed at low temperatures (Figure 4d), indicating the presence of deep defect states. Under saturation conditions with high excitation fluence, the intensity decreases in the order Ta_3N_5(Ta) >> Ta_3N_5(N) > Ta_3N_5(O), confirming reduced emission from deep defect states with increasing oxygen content and in line with the observed trend in sub-bandgap absorption. Considering all measurements, we conclude that low oxygen contents facilitate the high degree of structural order in Ta_3N_5(N) and Ta_3N_5(Ta) but lead to comparatively large concentrations of deep-level states that can have a pronounced impact on the optoelectronic properties of Ta_3N_5 thin films. In contrast, Ta_3N_5(O) is characterized by increased long-range structural disorder, but the high oxygen content leads to the beneficial elimination of deep-level defects.

To determine the impact of the different defect properties on charge separation and transfer, we performed a Kelvin probe and chopped voltammetry measurements for each of the different films (**Figure 5**). Contact potential differences (CPD) were measured in the dark and under illumination to determine the impact of defect properties on surface band bending and charge separation. For all Ta_3N_5 films, we observe a negative change in CPD upon excitation with the above bandgap illumination of 455 nm (Figure 5a), corresponding to a positive surface photovoltage (SPV). While this behavior is consistent with the n-type character of all investigated Ta_3N_5 films, the magnitude of the SPV depends on the synthetic route and associated defect content in the films. For Ta_3N_5(O), the SPV is ~200 meV, which is similar to or even larger than reported in previous studies.[3,11,30] In contrast, the magnitude of the SPV response is significantly reduced to <50 meV for both Ta_3N_5(N) and Ta_3N_5(Ta). Previously, higher SPV has been assigned to lower concentrations of deep-level defects, which reduces trapping and improves charge separation in the material.[11,30] Thus, these findings are consistent with the suppression of electronically active defect states with increasing oxygen content, as also observed by PDS and PL measurements, which enables the generation of a larger SPV.

To complement SPV measurements and gain insights into transient charge carrier trapping processes, we performed voltammetry measurements in 1 M KP_i with and without 0.1 M $K_4Fe(CN)_6$ under chopped illumination (Figure 5b,c; Figure S10, Supporting Information). Without a hole scavenger, large photocurrent transients are observed for all three photoelectrodes, with overshoots of approximately 80 μA cm^{-2}, 250 μA cm^{-2}, and 340 μA cm^{-2} at potentials >1 V versus RHE for Ta_3N_5(O), Ta_3N_5(N), and Ta_3N_5(Ta), respectively (Figure S10, Supporting Information). While these results indicate considerable interfacial charge trapping for all three electrodes, it is notable that the magnitude of the photocurrent transient is substantially smaller for Ta_3N_5(O), suggesting that this behavior is correlated with the deep-level defect content discussed above. Importantly, in the presence of 0.1 M $K_4Fe(CN)_6$, no transient photocurrent is observed for Ta_3N_5(O), as shown in Figure 5c. In contrast, both Ta_3N_5(N) and Ta_3N_5(Ta) are characterized by photocurrent transients upon illumination, even with hole scavenger in solution, with overshoots of approximately 25 μA cm^{-2} and 100 μA cm^{-2}, respectively, at potentials >1 V versus RHE. Taken together, these results indicate that interfacial charge transfer kinetics are much faster than charge trapping processes for the case of Ta_3N_5(O), but not for Ta_3N_5(N) and Ta_3N_5(Ta) due to the larger concentration of deep-level defects in these materials. While the presence of a sacrificial hole acceptor in solution decreases the degree of charge trapping in these films, it is not completely suppressed.

Overall, these results indicate a strong correlation between deep-level defect concentration, interfacial charge trapping, and photo-induced oxidation of Ta_3N_5 films. Based on these findings, we conclude that photocarrier trapping by deep-level defects impedes interfacial hole injection, even in the presence of a sacrificial hole acceptor, and facilitates oxidation of the interface (**Figure 6**). While high concentrations of deep-level defect states near the surface lead to rapid photooxidation of the material itself, the incorporation of oxygen impurities during synthesis can beneficially passivate deep-level defects and suppress such trapping processes. As a consequence, increased oxygen content enables kinetic stabilization (i.e., in the presence of a hole scavenger) of the surface and provides a viable route to the

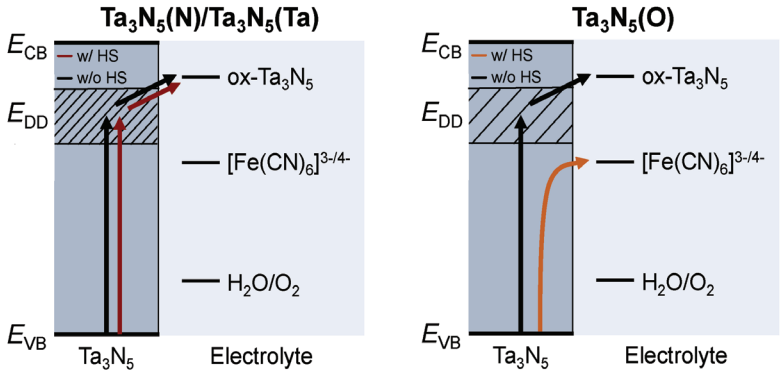

Figure 6. Schematic of the main kinetic pathways in the presence (w/ HS) and absence (w/o HS) of sacrificial hole acceptor. High concentrations of deep-level defects in Ta_3N_5 (N) and Ta_3N_5 (Ta) facilitate degradation via surface oxidation with (red arrow) and without (black arrow) hole scavenger. The beneficial passivation of deep-level defects in Ta_3N_5 (O) stabilizes the surface only in the presence of a hole acceptor (orange arrow). We note that the self-oxidation potential (ox-Ta_3N_5) of Ta_3N_5 is obtained from theoretical calculations[44] and can be subject to considerable uncertainties, and thus its position should only be considered qualitatively. The redox potential for $Fe(CN)_6^{4-}/Fe(CN)_6^{3-}$ and H_2O/O_2 are obtained from Ref.[55] E_{VB}, E_{DD}, and E_{CB} correspond to the potential of valence bands, deep defect states, and conduction bands.

enhanced long-term durability of Ta_3N_5 photoanodes. Beyond the kinetic stabilization described here using a sacrificial hole acceptor, it is expected that such defect-mediated mechanisms will also play a key role in defining the macroscopic stability of catalyst-functionalized or protected photoanodes.

3. Conclusion

In conclusion, we have demonstrated that (reactive) sputtering of thin film precursors with controlled oxygen and nitrogen concentrations, followed by ammonolysis, allows the fabrication of Ta_3N_5 thin films possessing differing degrees of structural disorder and tunable concentrations of shallow and deep-level defects that play a crucial role in defining their optical, electronic, and photoelectrochemical properties. In particular, by systematically analyzing the structural, compositional, optoelectronic, and photoelectrochemical properties of these thin films, we established a relationship between atomic-scale point defects and macroscale PEC stability. In Ta_3N_5(N) and Ta_3N_5(Ta), low oxygen contents facilitate long-range structural order but lead to high concentrations of deep-level states that play a dominant role in their optoelectronic properties. In contrast, Ta_3N_5(O) is characterized by reduced structural order but the high oxygen content leads to beneficial passivation of deep-level defects. Despite the different defect properties, the photocurrent densities of all three photoelectrodes degrade similarly under water oxidation conditions. However, material degradation does not lead to changes in surface morphology or appreciable dissolution of Ta. Rather, changes in surface composition before and after PEC testing reveal that photocurrent degradation is caused by the formation of a surface oxide layer that blocks interfacial hole injection and facilitates charge recombination, confirming that Ta_3N_5 is a self-passivating semiconductor. In contrast, Ta_3N_5(O) photoelectrodes exhibit long-term stability under ferrocyanide oxidation conditions, while both Ta_3N_5(Ta) and Ta_3N_5(N) experience immediate degradation under similar reaction conditions. These results indicate that shallow oxygen donors can be introduced into Ta_3N_5 to kinetically stabilize the interface, whereas deep-level defects result in rapid trapping of photocarriers and surface oxidation that renders kinetic stabilization strategies ineffective. Overall, these findings highlight the importance of tailoring point defects and foreign atom dopants in semiconductor photoelectrodes to not only enhance PEC performance characteristics but also increase stability via the application of kinetic stabilization strategies. Such insights are important for the rational development of corrosion protection and catalyst integration strategies on semiconductor photoelectrodes, particularly in the presence of defect states that are commonly found in thin film semiconductors.

4. Experimental Section

Synthesis of Ta_3N_5 Thin Films: All precursor thin films were deposited by reactive magnetron sputtering (PVD 75, Kurt J. Lesker) in a system with a base pressure of 5×10^{-8} Torr and a target-substrate distance of ~17 cm. The thin films were sputtered on n^+-type doped Si wafers (As doped, (100) oriented, Siegert Wafer GmbH) with a native oxide layer for PEC characterization and on fused silica (Siegert Wafer GmbH) for optical characterization. The silica substrates were cleaned by consecutively rinsing in DI water, acetone, and isopropanol, after which they were dried with flowing nitrogen.

For target conditioning, the Ta target (99.95%, Kurt J. Lesker) was first sputter-cleaned with a 60 W DC Ar plasma (99.9999%, Linde GmbH) for 15 min at a pressure of 8.5 mTorr with the substrate shutter closed. During the last 5 min, a 20 W RF substrate bias was applied to simultaneously sputter clean the substrates in situ prior to deposition. For TaO_x and TaN_x, the Ta target was sputtered in a gas mixture composed of Ar, N_2 (99.9999%, Linde GmbH), and O_2 (99.9999%, Linde GmbH) using a TruePlasma pulsed DC power supply. In detail, TaO_x films were sputtered for 13 min with an average power of 50 W, a substrate temperature of 500 °C, and a process pressure of 8.5 mTorr using an Ar atmosphere with 10% O_2 as the reactive gas. Prior to the introduction of O_2 to the process chamber and the deposition of TaO_x, a 5 nm thin Ta layer was deposited for 2 min to prevent oxidation of the substrate surface during the sputtering process. For this Ta interlayer, a sputtering power of 60 W, a substrate temperature of 500 °C, and a process pressure of 8.5 mTorr using an Ar flow rate of 40 sccm was used. TaN_x films were sputtered for 70 min with an average power of 50 W with active pulsed mode operating at 100 kHz with a 98% duty cycle, a substrate temperature of 650 °C, and a process pressure of 7 mTorr by adjusting the Ar, N_2, and O_2 flow rates to 10 sccm, 20 sccm, and 0.55 sccm, respectively. Ta films were sputtered for 18 min with a DC power of 60 W, a substrate temperature of 400 °C, and a process pressure

of 5.5 mTorr using an Ar flow rate of 25 sccm. During all depositions, the substrate holder was rotated at 10 rpm.

Following deposition, the sputtered precursor thin films were annealed in a quartz tube furnace (Nabertherm RS 80/300/1) with a constant NH_3 (99.999%, Linde GmbH) flow rate of 100 sccm at 1 bar pressure. The temperature was ramped up with a rate of 30 °C min^{-1}. After reaching 920 °C, the temperature was held constant for 3 h. Afterward, the furnace was turned off and the thin films were allowed to cool in a continuous flow of NH_3. To accelerate the cooling process, the clamshell of the furnace was opened once the temperature had reached <400 °C. At room temperature, the flow was switched to pure N_2 and the tube was purged for 10 min prior to removing the samples.

Structural and Compositional Characterization: The crystal structures and phase purities of the films were analyzed by GI-XRD (Rigaku SmartLab) using Cu K_α radiation at a 0.5° incidence angle. The 2θ diffraction angle was measured from 15° to 70° in increments of 0.05°.

The morphologies of the films were investigated using AFM (Bruker Dimension Icon). All AFM measurements were performed using the peak force tapping mode with a 2 kHz frequency and cantilevers with a spring constant of 3 N m^{-1}.

The near-surface compositions were analyzed by XPS (SPECS) using a non-monochromatized Al K_α source with an energy of 1486.6 eV and a PHOIBOS 100 concentric hemispherical energy analyzer. XPS binding energies were calibrated by shifting the C 1s core level to 284.8 eV. Data analysis was performed with CasaXPS software and the surface atomic composition was calculated using the corresponding peak area, atomic sensitivity factors, and an effective attenuation length escape depth correction.

ERDA was carried out at the Ion Beam Centre of Helmholtz-Zentrum Dresden-Rossendorf using a 43 MeV Cl^{7+} ion beam. The sample was positioned at an angle of 75° with respect to the incoming ion beam, with the scattering angle set to 30°. The area analyzed was ∼1.5 mm × 1.5 mm. The recoil atoms and scattered ions were detected with a Bragg ionization chamber, while hydrogen recoils were detected with a separate solid-state detector with a 25 µm Kapton foil in front of it, set at a scattering angle of 40°. The analysis of the measurements has been performed with the program NDF v9.3 g.[56]

XAS measurements were conducted at the Elettra Sincrotrone Trieste facility using the BEAR (Bending-magnet Emission Absorption Reflection) beamline to investigate the N-K-edge absorption of the samples. For these measurements, the energy range was divided into three regions: 380 eV to 392 eV with a step of 0.25 eV, 392.05 eV to 415 eV with a step of 0.05 eV, and 415.2 eV to 450 eV with a step of 0.2 eV. Two scans were performed for each sample, with an integration time of 0.4 s per step.

Optical Characterization: The crystal structure and quality were analyzed using a home-built Raman setup with a 532 nm excitation wavelength in continuous wave mode. The scattered light was filtered with a 532 nm long-pass filter to minimize Rayleigh scattering and was analyzed using a Horiba iHR 550 spectrometer (2400 mm^{-1} grating) and a Horiba Symphony II charge-coupled device (CCD) camera. The spectra were recorded in the range of 100 – 1000 cm^{-1} at room temperature. Additionally, the Andor Kymera spectrograph was used for photoluminescence spectroscopy measurements. The spectrograph is paired with an Andor iDus 416 CCD detector. This setup was used for PL spectroscopy, employing a 300 mm^{-1} grating and a 403 nm excitation source. The reflected light was filtered with a 410 nm long-pass filter. All PL measurements were performed in a liquid-flow cryostat under vacuum conditions and at temperatures between 10 K and 300 K.

Both the above- and sub-bandgap absorption were quantified using a home-built PDS system. The photoelectrodes were immersed in perfluorohexane and illuminated by a chopped (9 Hz) monochromatized halogen light source (250 W) at normal incidence. The absorbance was measured in the range of 400 – 1200 nm using a 635 nm laser diode as the probe beam, the deflection of which was monitored by a segmented detector. The signal was read out using a lock-in amplifier (Stanford Research SRS 530).

CPD and SPV measurements were performed using a commercial KP020 Kelvin probe system from KP Technology under ambient conditions. For illumination, a 455 nm Thorlabs LED operated at 5 mW cm^{-2} was used to reach SPV signal saturation.

Photoelectrochemical Measurements: The PEC performance characteristics and stability of Ta_3N_5 thin films on Si substrates were determined by linear sweep voltammetry and chronoamperometry, respectively, using a Biologic (SP-300) potentiostat. A photoelectrochemical cell in a three-electrode configuration was used with an Ag/AgCl reference electrode (3 M NaCl), a Ta_3N_5 photoanode as the working electrode, and a Pt wire as the counter electrode. All PEC experiments were conducted in a 1 M potassium phosphate (KP_i) buffer at pH 12.3 with and without 0.1 M $K_4Fe(CN)_6$ as a sacrificial hole acceptor. Prior to the photoelectrochemical experiments, the electrolyte was degassed by bubbling with Ar (99.9999% Linde GmbH) for 10 min. A solar simulator (Ashai, AM 1.5G) was used for front-side illumination and was adjusted to 100 mW cm^{-2}. Linear sweep voltammetry was performed by sweeping the potential from 0.4 V to 1.6 V versus RHE under constant or chopped illumination, as well as in darkness. Chronoamperometry was conducted at 1.23 V versus RHE under constant illumination for 1 h.

ICP-MS (Agilent 7900) was used to determine the Ta concentration in the electrolyte after 1 h chronoamperometry measurements in 1 M KPi (pH 12.3) with and without 0.1 M $K_4Fe(CN)_6$ at 1.23 V versus RHE. The system was equipped with a perfluoroalkoxy alkane (PFA) inert sample introduction system. All measurements were conducted in He-collision mode and a high matrix introduction mode with 0.15 L min^{-1} Ar dilution. Prior to the measurement, the electrolyte samples were pre-diluted in a 1:20 ratio with a mixture of 2% HNO_3 and 0.5% HCl, prepared respectively from 70% and 35% concentrated acids (both CarlRoth, ROTIPURAN Supra, <1 ppb trace metals) and 18.2 MΩcm deionized water. The Ta calibration series was freshly prepared from a certified multielement standard (TraceCERT, transition metal mix 2) using the same mixture of 2% HNO_3 and 0.5% HCl. During the ICP-MS measurement, an internal standard containing rare earth elements was added to verify measurement stability across all thin films.

Supporting Information

Supporting Information is available from the Wiley Online Library or from the author.

Acknowledgements

J.E. acknowledges funding by the Deutsche Forschungsgemeinschaft (DFG, German Research Foundation) – Grant No. 428591260. J.E. and V.S. acknowledge support from the Bavarian Academy of Sciences and Humanities. The authors further acknowledge support from the European Research Council (ERC) under the European Union's Horizon 2020 research and innovation program (grant agreement no. 864234), the Deutsche Forschungsgemeinschaft (DFG, German Research Foundation) under Germany's Excellence Strategy – EXC 2089/1 – 390776260, and TUM.Solar in the context of the Bavarian Collaborative Research Project Solar Technologies Go Hybrid (SolTech). The authors acknowledge Elettra Sincrotrone Trieste for providing access to its synchrotron radiation facilities and the authors thank Angelo Giglia and Stefano Nannarone for assistance in using beamline BEAR. Furthermore, the authors acknowledge HZDR (Dresden-Rossendorf, Germany) for the provision of experimental facilities. Parts of this research were carried out at the Ion Beam Center. S.S. acknowledges support from the Alexander von Humboldt Foundation.

Open access funding enabled and organized by Projekt DEAL.

Conflict of Interest

The authors declare no conflict of interest.

Data Availability Statement

The data that support the findings of this study are available from the corresponding author upon reasonable request.

Keywords

defects, stability, Ta_3N_5 photoelectrodes, thin films, water splitting

Received: March 31, 2024
Revised: June 14, 2024
Published online: July 10, 2024

[1] J. H. Montoya, L. C. Seitz, P. Chakthranont, A. Vojvodic, T. F. Jaramillo, J. K. Nørskov, *Nat. Mater.* **2017**, *16*, 70.
[2] A. Zakutayev, *J. Mater. Chem. A* **2016**, *4*, 6742.
[3] L. I. Wagner, E. Sirotti, O. Brune, G. Grötzner, J. Eichhorn, S. Santra, F. Munnik, L. Olivi, S. Pollastri, V. Streibel, I. D. Sharp, *Adv. Funct. Mater.* **2024**, *34*, 2306539.
[4] C.-M. Jiang, L. I. Wagner, M. K. Horton, J. Eichhorn, T. Rieth, V. F. Kunzelmann, M. Kraut, Y. Li, K. A. Persson, I. D. Sharp, *Mater. Horiz.* **2021**, *8*, 1744.
[5] T. Takata, C. Pan, K. Domen, *Sci. Technol. Adv. Mater.* **2015**, *16*, 033506.
[6] W.-J. Chun, A. Ishikawa, H. Fujisawa, T. Takata, J. N. Kondo, M. Hara, M. Kawai, Y. Matsumoto, K. Domen, *J. Phys. Chem. B* **2003**, *107*, 1798.
[7] R. Liu, Z. Zheng, J. Spurgeon, X. Yang, *Energy Environ. Sci.* **2014**, *7*, 2504.
[8] A. A. Haleem, S. Majumder, N. Perumandla, Z. N. Zahran, Y. Naruta, *J. Phys. Chem. C* **2017**, *121*, 20093.
[9] Y. He, J. E. Thorne, C. H. Wu, P. Ma, C. Du, Q. Dong, J. Guo, D. Wang, *Chem* **2016**, *1*, 640.
[10] A. Dabirian, R. van de Krol, *Appl. Phys. Lett.* **2013**, *102*, 033905.
[11] J. Fu, F. Wang, Y. Xiao, Y. Yao, C. Feng, L. Chang, C.-M. Jiang, V. F. Kunzelmann, Z. M. Wang, A. O. Govorov, I. D. Sharp, Y. Li, *ACS Catal.* **2020**, *10*, 10316.
[12] J. Eichhorn, S. P. Lechner, C.-M. Jiang, G. F. Heunecke, F. Munnik, I. D. Sharp, *J. Mater. Chem. A* **2021**, *9*, 20653.
[13] G. Fu, S. Yan, T. Yu, Z. Zou, *Appl. Phys. Lett.* **2015**, *107*, 171902.
[14] Y. Xie, Y. Wang, Z. Chen, X. Xu, *ChemSusChem* **2016**, *9*, 1403.
[15] Y. Pihosh, T. Minegishi, V. Nandal, T. Higashi, M. Katayama, T. Yamada, Y. Sasaki, K. Seki, Y. Suzuki, M. Nakabayashi, M. Sugiyama, K. Domen, *Energy Environ. Sci.* **2020**, *13*, 1519.
[16] Y. Pihosh, V. Nandal, R. Shoji, R. Bekarevich, T. Higashi, V. Nicolosi, H. Matsuzaki, K. Seki, K. Domen, *ACS Energy Lett.* **2023**, *8*, 2106.
[17] T. Higashi, H. Nishiyama, V. Nandal, Y. Pihosh, Y. Kawase, R. Shoji, M. Nakabayashi, Y. Sasaki, N. Shibata, H. Matsuzaki, K. Seki, K. Takanabe, K. Domen, *Energy Environ. Sci.* **2022**, *15*, 4761.
[18] L. Wang, F. Dionigi, N. T. Nguyen, R. Kirchgeorg, M. Gliech, S. Grigorescu, P. Strasser, P. Schmuki, *Chem. Mater.* **2015**, *27*, 2360.
[19] T. Higashi, Y. Sasaki, Y. Kawase, H. Nishiyama, M. Katayama, K. Takanabe, K. Domen, *Catalysts* **2021**, *11*, 584.
[20] J. Fu, Z. Fan, M. Nakabayashi, H. Ju, N. Pastukhova, Y. Xiao, C. Feng, N. Shibata, K. Domen, Y. Li, *Nat. Commun.* **2022**, *13*, 729.
[21] X. Zou, X. Han, C. Wang, Y. Zhao, C. Du, B. Shan, *Sustainable Energy Fuels* **2021**, *5*, 2877.
[22] Y. Xiao, Z. Fan, M. Nakabayashi, Q. Li, L. Zhou, Q. Wang, C. Li, N. Shibata, K. Domen, Y. Li, *Nat. Commun.* **2022**, *13*, 7769.
[23] Y. Wang, D. Zhu, X. Xu, *ACS Appl. Mater. Interfaces* **2016**, *8*, 35407.
[24] K. Li, B. Miao, W. Fa, R. Chen, J. Jin, K. H. Bevan, D. Wang, *ACS Appl. Mater. Interfaces* **2021**, *13*, 17420.
[25] Y. Xiao, C. Feng, J. Fu, F. Wang, C. Li, V. F. Kunzelmann, C.-M. Jiang, M. Nakabayashi, N. Shibata, I. D. Sharp, K. Domen, Y. Li, *Nat. Catal.* **2020**, *3*, 932.
[26] S. Youn Chae, E. Duck Park, *Appl. Surf. Sci.* **2022**, *583*, 152566.
[27] J. Wang, J. Feng, L. Zhang, Z. Li, Z. Zou, *Phys. Chem. Chem. Phys.* **2014**, *16*, 15375.
[28] J. Wang, A. Ma, Z. Li, J. Jiang, J. Feng, Z. Zou, *Phys. Chem. Chem. Phys.* **2015**, *17*, 23265.
[29] Y. Li, T. Takata, D. Cha, K. Takanabe, T. Minegishi, J. Kubota, K. Domen, *Adv. Mater.* **2013**, *25*, 125.
[30] C. Shao, R. Chen, Y. Zhao, Z. Li, X. Zong, C. Li, *J. Mater. Chem. A* **2020**, *8*, 23274.
[31] E. Nurlaela, M. Harb, S. del Gobbo, M. Vashishta, K. Takanabe, *J. Solid State Chem.* **2015**, *229*, 219.
[32] A. Dabirian, R. van de Krol, *Chem. Mater.* **2015**, *27*, 708.
[33] I. Narkeviciute, T. F. Jaramillo, *Sol. RRL* **2017**, *1*, 1700121.
[34] H. X. Dang, N. T. Hahn, H. S. Park, A. J. Bard, C. B. Mullins, *J. Phys. Chem. C* **2012**, *116*, 19225.
[35] D. Yokoyama, H. Hashiguchi, K. Maeda, T. Minegishi, T. Takata, R. Abe, J. Kubota, K. Domen, *Thin Solid Films* **2011**, *519*, 2087.
[36] M. Rudolph, I. Vickridge, E. Foy, J. Alvarez, J.-P. Kleider, D. Stanescu, H. Magnan, N. Herlin-Boime, B. Bouchet-Fabre, T. Minea, M.-C. Hugon, *Thin Solid Films* **2019**, *685*, 204.
[37] Y. Lee, K. Nukumizu, T. Watanabe, T. Takata, M. Hara, M. Yoshimura, K. Domen, *Chem. Lett.* **2006**, *35*, 352.
[38] S. J. Henderson, A. L. Hector, *J. Solid State Chem.* **2006**, *179*, 3518.
[39] T. Jing, Y. Dai, X. Ma, W. Wei, B. Huang, *RSC Adv.* **2015**, *5*, 59390.
[40] X. Wang, H. Huang, T. Fang, J. Feng, Z. Li, Z. Zou, *J. Phys. Chem. C* **2019**, *123*, 28763.
[41] Y. He, P. Ma, S. Zhu, M. Liu, Q. Dong, J. Espano, X. Yao, D. Wang, *Joule* **2017**, *1*, 831.
[42] Ø. Dahl, M. F. Sunding, V. Killi, I.-H. Svenum, M. Grandcolas, M. Andreassen, O. Nilsen, A. Thøgersen, I. J. T. Jensen, A. Chatzitakis, *ACS Catal.* **2023**, *13*, 11762.
[43] H. Gerischer, *J. Electroanal. Chem. Interf. Electrochem.* **1977**, *82*, 133.
[44] S. Chen, L.-W. Wang, *Chem. Mater.* **2012**, *24*, 3659.
[45] Y. Zhang, W. Han, L. Ding, F. Fang, Z. Xie, X. Liu, K. Chang, *Catal. Sci. Technol.* **2022**, *12*, 4040.
[46] L. Zheng, M. Wang, Y. Li, F. Ma, J. Li, W. Jiang, M. Liu, H. Cheng, Z. Wang, Z. Zheng, P. Wang, Y. Liu, Y. Dai, B. Huang, *Nanomater.* **2021**, *11*, 2404.
[47] J. Wang, T. Fang, L. Zhang, J. Feng, Z. Li, Z. Zou, *J. Catal.* **2014**, *309*, 291.
[48] E. Nurlaela, S. Ould-Chikh, M. Harb, S. del Gobbo, M. Aouine, E. Puzenat, P. Sautet, K. Domen, J.-M. Basset, K. Takanabe, *Chem. Mater.* **2014**, *26*, 4812.
[49] J. Wang, A. Ma, Z. Li, J. Jiang, J. Feng, Z. Zou, *Phys. Chem. Chem. Phys.* **2015**, *17*, 8166.
[50] J. Xiao, J. J. M. Vequizo, T. Hisatomi, J. Rabeah, M. Nakabayashi, Z. Wang, Q. Xiao, H. Li, Z. Pan, M. Krause, N. Yin, G. Smith, N. Shibata, A. Brückner, A. Yamakata, T. Takata, K. Domen, *J. Am. Chem. Soc.* **2021**, *143*, 10059.
[51] A. Jain, S. P. Ong, G. Hautier, W. Chen, W. D. Richards, S. Dacek, S. Cholia, D. Gunter, D. Skinner, G. Ceder, K. A. Persson, *APL Mater.* **2013**, *1*, 011002.
[52] A. Arranz, C. Palacio, J. Avila, *Phys. Rev. B* **2005**, *71*, 035405.
[53] N. Pandey, M. Gupta, D. M. Phase, A. Gupta, *J. Synchrotron Rad.* **2021**, *28*, 1504.
[54] A. Soudi, E. H. Khan, J. T. Dickinson, Y. Gu, *Nano Lett.* **2009**, *9*, 1844.
[55] W. M. Haynes, *CRC Handbook of Chemistry and Physics (92nd ed.)*, CRC Press, Boca Raton, FL, **2011**.
[56] N. P. Barradas, C. Jeynes, R. P. Webb, *Appl. Phys. Lett.* **1997**, *71*, 291.